3-D Microstructure Analysis of Fuel Cell Materials: Spatial Distributions of Tortuosity, Void Size and Diffusivity

A. Çeçen,[a,b] E. A. Wargo,[a,b,*] A. C. Hanna,[a,b] D. M. Turner,[b] S. R. Kalidindi,[b] and E. C. Kumbur[a,**,z]

[a]*Electrochemical Energy Systems Laboratory and* [b]*Mechanics of Microstructures Group, Department of Mechanical Engineering and Mechanics, Drexel University, Philadelphia, Pennsylvania 19104, USA*

Due to the minute length scales and heterogeneous nature of fuel cell components, experimental quantification of the key properties of these materials can be expensive and quite difficult to conduct, if not impossible. The objective of this work is to introduce 3-D microstructure analysis tools for "direct" quantification of the key structure-related transport measures of porous fuel cell materials. Two important microstructure analysis tools are presented for the evaluation of tortuosity and void (i.e., pore) size distribution. The first tool is aimed at quantification of the tortuosity distribution in an internal structure using a shortest path search method. The second tool is aimed at quantification of orientation-resolved chord length distributions of a phase (e.g., void, solid) in a given 3-D microstructure dataset to extract the orientation and size related statistics of a selected phase. Various other key structure metrics (e.g, phase-specific volume fraction, phase connectivity, internal surface area etc.) are also successfully extracted by using these tools. Additionally, a 3-D diffusion model is presented to determine the effective structural diffusivity coefficient based on the measured microstructure. For demonstration purposes, these methods are applied to the measured microstructure datasets of the micro-porous layer of a polymer electrolyte fuel cell.
© 2012 The Electrochemical Society. [DOI: 10.1149/2.068203jes] All rights reserved.

The performance and durability of fuel cells are strongly linked to the materials used in these systems.[1] However, experimental quantification of the key properties of these materials can be expensive and quite difficult to conduct, if not impossible. For example, one major issue which continues to hinder polymer electrolyte fuel cell (PEFC) development is water management.[1–9] Nearly every PEFC component plays an important role in water management. In order to better understand the transport characteristics of the key fuel cell components, a comprehensive understanding of the complex internal structure of these materials is needed.

To date, most standard experimental methods (e.g., porometric techniques) are limited to providing bulk property data which only indicate the general characteristics of the material. However, many of the fuel cell materials exhibit strong heterogeneity with anisotropy in the properties, whose rigorous quantification requires measurements in multiple directions and locations. Moreover, small variations in the manufacturing process can lead to significant changes in the bulk properties of these materials due to the possible changes in the internal structure (henceforth referred to as "microstructure"). Therefore, it is imperative to develop microstructure analysis tools to accurately capture the myriad features and spatial variations of the key transport properties in these materials.

Recently, various microscale analysis techniques have emerged to obtain insights into the precise roles of morphological features of fuel cell materials on their bulk transport properties.[10–20] These techniques typically start with a detailed representation of the internal structure of fuel cell materials to better understand their internal structure and related effects on the performance of fuel cells. To date, most studies utilize focused ion beam scanning electron microscopy (FIB-SEM) or X-ray computed tomography (XCT) to extract 3-D microstructure datasets. These datasets have been utilized in a range of numerical models to evaluate the transport properties of key fuel cell materials. For instance, Gunda et al.[10] used FIB-SEM to quantify the microstructure of a solid oxide fuel cell (SOFC) cathode, and extracted effective transport coefficients for gas diffusivity by utilizing a Fickian diffusion model. Similarly, Ostadi et al.[11] analyzed the micro-porous layer (MPL) and macro diffusion media (macro-DM) substrate of a dual-layer DM sample using FIB-SEM and XCT, respectively. A lattice-Boltzmann (LB) model was applied to the measured microstructure to determine the effective gas diffusion coefficients. Very recently, Becker et al.[12] approximated the gas diffusivity of a DM sample with a Fickian diffusion model applied on an XCT dataset. While these studies present useful tools for the estimation of some key transport properties, the direct evaluation of key structural parameters (henceforth referred to as "metrics") and their spatial variation is generally overlooked.

A major impediment to "direct" quantification of the key structure metrics and their spatial variation within the microstructure of fuel cell materials arises from the lack of: (i) rigorous definitions for the structure metrics of interest in fuel cell materials, and (ii) computationally efficient protocols for extracting these metrics from the measured datasets. In the context of this paper, "direct" implies that the analysis method is free of geometrical and physical assumptions (e.g., semi-empirical correlations). To date, fundamental image analysis techniques have been widely used to estimate common metrics including phase-specific volume fraction (e.g., porosity), connectivity, and internal surface area of complex materials. However, the direct methods or computational protocols to estimate the tortuosity and void (i.e., pore) size distribution are more vaguely mentioned in literature. For example, Ostadi et al.[11] utilized the effective diffusivity results from the LB simulation to estimate average tortuosity values for the MPL, and Iwai et al.[13] performed a similar procedure to determine the effective tortuosity of an SOFC anode. Notably, Wu et al.[14] introduced a method based on a modified A* search algorithm to find relative path lengths as a measure for tortuosity in digitally reconstructed sodium chloride compacts. The approach is based on the wave-front propagation method, and enables direct evaluation of a "geometric" tortuosity without utilizing an effective diffusivity coefficient-tortuosity relation as in Refs. 11 and 13. While this method brings a new perspective to evaluate the tortuosity, it is limited to performing analysis in 2-D datasets, and therefore is not capable of capturing the bidirectional transport in a 3-D microstructure dataset. Similarly, Zils et al.[15] utilized a geometric method to calculate the tortuosity of PEFC catalyst layer (CL) samples, but the approach yields an estimate of only a single "average" value for tortuosity. Given the highly heterogeneous and complex internal structures of fuel cell materials, defining a single value to represent the tortuous nature of the fuel cell materials is highly questionable. Instead, an appropriate approach would be to determine the spatial variation of tortuous paths for a given 3-D microstructure dataset and represent the tortuosity as a "distribution" (i.e., probability density of finding tortuous paths of different lengths).

Recently, Fishman and Bazylak[16] calculated the through-plane tortuosity distributions of DM samples using the measured porosity distribution with the Tomadakis and Sotirchos approximation. Notably, Haussener et al.[17] presented a method for obtaining tortuosity distributions in 3-D by solving the continuity and Navier-Stokes equations to determine a large number of stream lines which represent the tortuous paths. Lindquist et al.[18] resolved tortuosity distribution by determining the shortest paths through the medial axis of the pore network in 3-D; however, this approach restricts transport to the medial axis of a pore which might not well-represent the transport phenomena in fuel cell materials. Another promising approach for determining tortuosity distribution has been presented by Axelsson and Svensson.[19] The method relies on an adaptation of the pore skeleton approach commonly used in porous media literature, in which the 3-D pore structure is broken down into individual pores based on distance transformations. While a single connecting pathway (similar to a medial axis) between adjacent pores can be identified, this approach also confines transport to only the central skeleton and does not account for the remaining voxels of the pore space. Due to the complex and jagged geometry of fuel cell materials like the MPL and catalyst layer, it is anticipated that a purely voxel-based approach would be more appropriate to better capture the myriad details of true morphology of the complex fuel cell materials. To date, such a microstructure-resolved approach that enables *direct* quantification of the tortuosity distribution (e.g., without using a semi-empirical approximation or physical/geometrical assumptions) in a 3-D microstructure dataset has not been reported.

Another key structure metric of interest in fuel cell materials is the void (i.e., pore) size distribution. To date, the most common approach for quantifying the void size distribution in these materials is based on idealizing the void space as a series of connected spheres. Mapping the complex internal structure of the actual fuel cell materials to such an idealized geometry is not only highly questionable, but its ability to preserve the bulk transport properties of interest is highly improbable. For instance, a recent effort by Zielger et al.[20] reports the use of an idealized geometry approach to determine the void size distribution of the PEFC catalyst layer. While the approach enables accurate analysis of homogenous porous structures in 3-D, the use of connected spherical geometries to quantify the void space most likely misrepresents the jagged morphology of complex fuel cell materials such as in the catalyst layer or DM. A direct approach that quantifies the true variation in geometrical shape and size of the void space in fuel cell materials has yet to be reported or presented.

The focus of this paper is to introduce *direct* methods for extracting key structure related transport metrics of fuel cell materials without using semi-empirical approximations or physical/geometrical assumptions, to enable better understanding of the structure of fuel cell materials. Two microstructure analysis protocols are presented for the quantification of the tortuosity and void size distributions. Firstly, a shortest path search method is developed to identify all of the tortuous paths and compute the spatial distribution of tortuosity for a given microstructure dataset. Secondly, an alternative method is presented to quantify the statistics of the connected-void space using orientation-resolved chord length distributions to accurately quantify the void geometry and size distribution. A chord is simply defined as a line segment that lies completely in the desired phase (e.g., void or solid). The computational protocols described here allow for the identification of all the chords that could be placed in a selected orientation in a given microstructure to capture the size and geometry of any phase. Additionally, a 3-D diffusion model is developed to calculate the "specific" effective structural diffusivity coefficient for a given microstructure. In an effort to demonstrate their potential utility, these methods are applied to the MPL of a PEFC.

Methods and Computational Procedures

Dataset acquisition and image processing.— The MPL of a SIGRACET SGL 10BC gas diffusion layer was selected for initial demonstration of the presented methods. Due to the relatively small void sizes, FIB-SEM[10,11,13,15,20,21] was chosen to capture the inter-
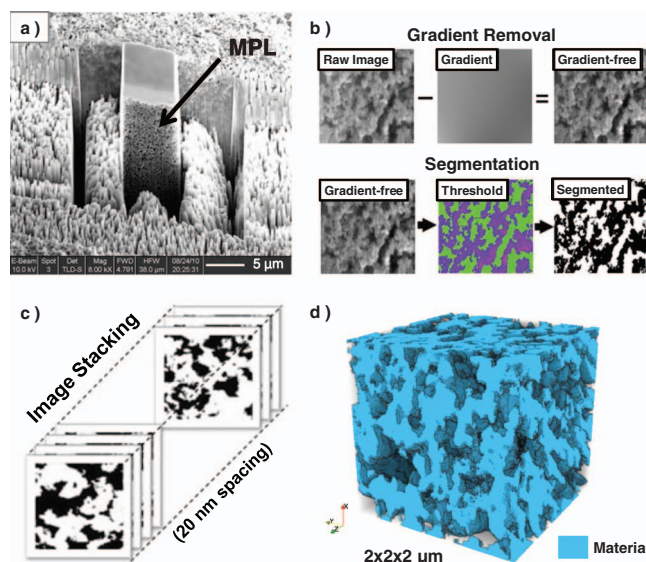

Figure 1. Data acquisition and reconstruction process: a) serial sectioning of MPL using FIB-SEM; b) image processing to remove shadow gradients and perform segmentation; c) stacking of segmented images; and d) the 3-D reconstruction of the MPL.

nal structure of the tested MPL sample in 3-D. An FEI Strata DB 235 FIB-SEM was utilized to quantify/characterize an MPL volume of ~5 × 8 × 2 μm by serial sectioning with an image resolution of ~10 nm and slice thickness of 20 nm. A 1.5 μm platinum layer was deposited over the volume of interest prior to serial sectioning to prevent ion damage, and the volume of interest was exposed as a peninsula to reduce shadows in the images (Fig. 1a). During the imaging process, the void structure of the tested MPL sample has not been impregnated with low-contrast resin as in[13] due to the fragile nature of the MPL. However, as also demonstrated in Refs. 10, 11, 15, 20, and 21, key volumetric information was able to be captured from the acquired SEM images without impregnation of the tested MPL sample.

During image acquisition, beam shift and/or sample drift can cause misalignment between consecutive images. To remove these effects, the image stack was re-aligned using a discrete Fourier transform registration code. All images in the stack were then shifted down and stretched vertically to correct for the projection effects due to imaging with the SEM source angled at 52°. As a final step, the shadow gradient in each image was removed by finding a bi-parabolic fit for the gradient and dividing the image data by the fitted bi-parabolic surface (Fig. 1b). The bi-parabolic fit for each image was computed using the surface fitting method proposed by Pastushenko.[22]

Several thresholding techniques have been tested to accurately distinguish the void pixels from the material pixels in each SEM image. Among the tested techniques, the iterative ISODATA method[23–25] was selected for segmentation (Fig. 1b), as it yielded the best segmentation upon visual inspection, resulting in a porosity value which is in good agreement with literature.[11,12,26,27] Furthermore, the iterative ISODATA method was implementable in an automated fashion, which is highly beneficial for segmenting the large stacks of images which result from FIB-SEM. Once the images were segmented, the resulting images were then stacked to create a 3-D binary image (i.e., digital structure dataset) of the internal structure of the MPL sample (Fig. 1c). This 3-D structure dataset was then further analyzed to remove any material islands (i.e., residuals) that appear to be floating in void space. Typically less than a few voxels in size, these islands are attributed to noise in the SEM images. For all segmentation methods tested, island removal only converted less than 0.2% of the volume of the dataset into voids. The resulting binary 3-D structure dataset (example shown in Fig. 1d) was used to determine key structure metrics of the MPL (e.g., porosity, connectivity, surface area, tortuosity
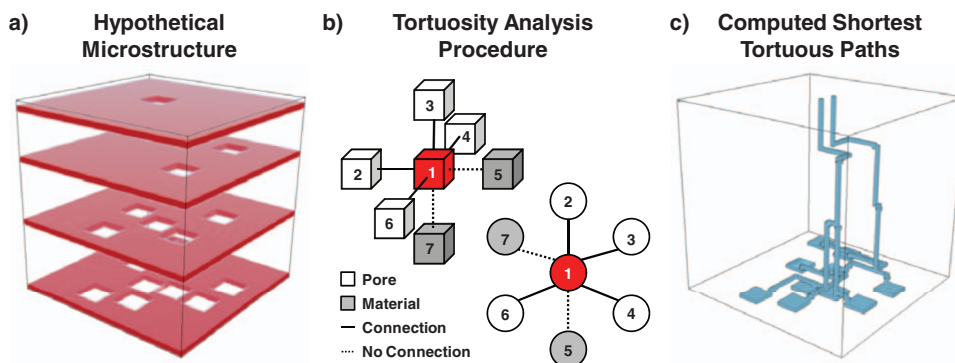
Figure 2. a) Hypothetical structure; b) Procedure for the tortuosity analysis; and c) For the given hypothetical microstructure, the computed shortest tortuous paths from the bottom surface openings to the top surface.

distribution, chord-length distributions etc). More detailed information regarding the dataset acquisition and image processing procedures may be found in our publication.[21]

Quantification of porosity, surface area and connectivity.— As a first step in determining key structure metrics of the MPL, fundamental image analysis techniques were applied to estimate phase-specific volume fraction (e.g., porosity), total internal surface area, and connectivity. Porosity was estimated as the ratio of the number of void voxels to the total number of voxels in the 3-D MPL microstructure dataset. Next, total surface area was estimated using matrix shifting to detect boundaries in directions along the main axes. The boundary detection was performed separately for positive and negative directions on the same axis, resulting in a total of six directions (henceforth referred to as "primary directions"). For each primary direction, the number of boundary voxels identified in that direction was multiplied by the surface area of a voxel face. The resulting surface area values for the six directions were summed and then divided by the size of the analyzed volume to estimate the surface area per unit volume. Subsequently, connectivity was estimated by identifying the connected components within the void space. Any void voxels that are connected to both the starting surface and the destination surface in the through-plane direction were identified as the "connected-void" phase. The ratio of the number of connected-void voxels to the total number of void voxels was defined as the void connectivity. This method also allows for reconstruction of the through-plane connected void network in 3-D, from which the connected surface area per unit volume can be determined.

Determination of tortuous paths and tortuosity distribution.— A tortuous path is defined here as the shortest path that starts at any surface voxel on one side of the structure dataset and reaches the opposing side while always remaining in a connected material phase (e.g., void). Each tortuous path is then assigned a tortuosity measure, which is simply the ratio of the actual path length to the shortest distance between the opposing surfaces of interest. It is therefore a directional metric, and can be anisotropic. It captures the difficulty of enabling transport in the given direction due to the presence of convoluted pathways. A major limitation of defining a single tortuosity value is that it does not capture the details of the geometry of the cross-section associated with each path. As such, although it effectively captures an important aspect of the transport path, it is not a complete metric since it cannot predict the effective bulk transport properties in the complete space of all possible internal structure topologies.

A special algorithm was developed to identify all of the tortuous paths existing within a selected 3-D digital microstructure dataset. This method uses Dijkstra's algorithm[28] to search for the shortest path from an entry point on the start surface to any point on the end surface. To implement this approach, the given 3-D structure dataset is transformed into a 2-D adjacency matrix, where the structure is treated

as a mathematical graph (Fig. 2b). Each node in the graph represents a voxel (i.e., void or solid in the case of the MPL), and each link represents the physical connectivity between the two voxels. The link between any two void voxels has a numerical value representing the Euclidean distance between the two. The search algorithm then finds the shortest possible path from a designated starting node to any end node on the opposing surface. Performing the shortest path calculation for every single void voxel on the start surface automatically identifies all of the tortuous paths of interest (Fig. 2c). In Fig. 2, the start and end ("destination") surfaces are the bottom and top surfaces of the hypothetical microstructure dataset, respectively. The length of each tortuous path is then divided by the height (thickness) of the selected microstructure volume to estimate the corresponding tortuosity values. For the tested MPL microstructure, the travel from an entry point on the starting surface to a point in the destination surface was assumed to occur only along the orthogonal axes, and only transport through the void phase was allowed. However it is possible to modify this method to enable travel in more directions or through different phases.

The tortuosity distribution obtained using this method can be used to determine various tortuosity related statistics (e.g., mean, median, mode, standard deviation). To the best of the authors' knowledge, this is the first development of a "direct" method which can be applied directly on the voxelated structure for the determination of a tortuosity distribution in a 3-D microstructure dataset. It is anticipated that the large quantity of statistics obtained using this approach will lead to a deeper insight into the precise role of this key structure metric in influencing the bulk transport properties, and allow for more detailed evaluation of microstructure. It is important to note that the presented tortuosity approach enables identification of the "existing" pathways available for transport within the measured microstructure, and was intentionally designed to be independent of any empirical correlations and physical assumptions (e.g., particle size, length scale). In order to determine the preferable pathways (among the existing pathways) that a species will move through, one must rely on a condition-specific physical model that properly describes the transport-related problem under investigation. The approach presented herein can be used to define a simple yet robust tortuosity metric which can be used to correlate the measured microstructure with the structure-related transport properties.

Chord length distribution – an alternative concept for void size distribution.— In general, the void (i.e., pore) size distribution quantifies the relative abundance of each particular void size in a given volume, where the "size" is defined as the effective diameter of a void in the plane normal to the direction of travel within that void. Since fuel cell materials contain connected void networks rather than isolated voids with clear boundaries, the identification of a void requires the use of artificial or idealized geometrical shapes. Consequently, while an idealized pore may have a descriptive void size (e.g., radius of a cylinder), an actual void network in most cases cannot be
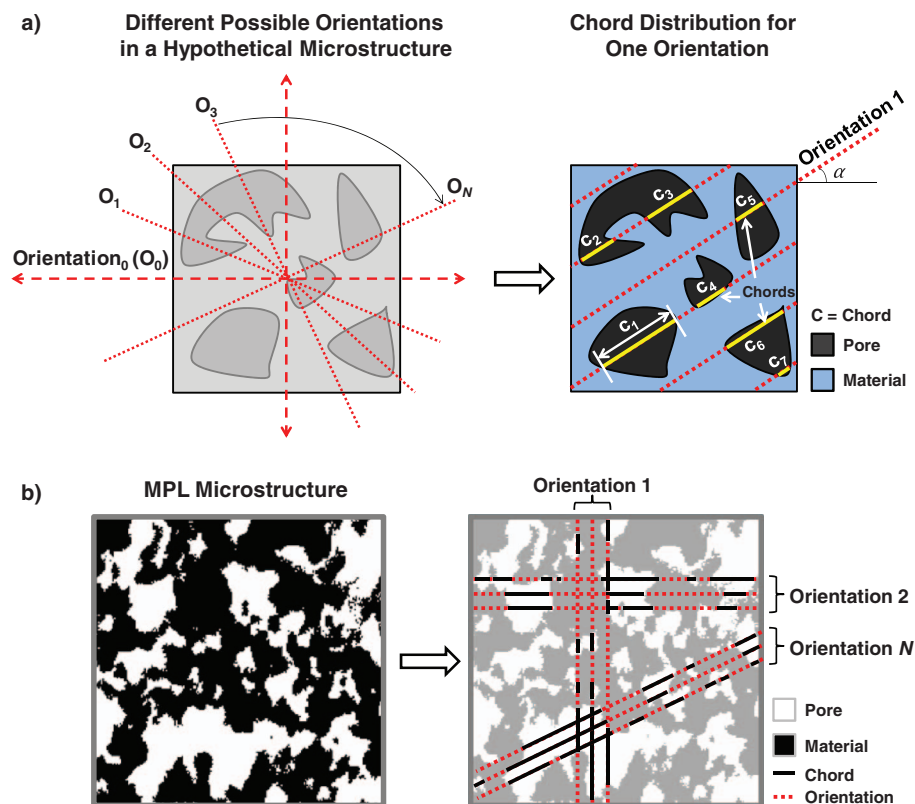
Figure 3. a) A hypothetical microstructure with chords of length 'c_i' drawn using an orientation with angle α. b) Demonstration of chord lengths in the MPL microstructure data for several possible orientations.

described by a single void size. Instead, the actual "void" has to be described by multiple void sizes that may or may not overlap due to the 3-D nature of the complex pore architecture. Therefore, while the void size for an idealized microstructure can be well-defined, the concept of defining a void and its size becomes ambiguous for a complex microstructure, especially for those seen in fuel cell materials.

Here, we present the concept of the chord length distribution[19,29] as an alternative parameter to the commonly used void size distribution concept in order to better represent the shape and size distribution of the void space in complex fuel cell microstructures like the MPL. The chord length analysis procedure presented herein is also closely related to the angularly resolved lineal path function described in Ref. 30. A chord is defined as a line of specific orientation which connects two phase boundaries within a material structure while lying completely within a single material phase (Fig. 3a). Therefore, the start and end points of a chord are located at the phase boundaries and form a pair of points that define the chord for a given orientation. Figure 3 shows this concept using a hypothetical microstructure and a single chord orientation (Fig. 3a), and demonstrates the extension to an actual microstructure such as the MPL using several chord orientations (Fig. 3b). The length 'c' of a chord is estimated by the Euclidean distance between the boundary pixel pair. This operation is repeated for desired directions and phases throughout every boundary pixel pair to produce a chord length dataset, which represents the chord length distribution.

The chord length distribution described above presents a much more rigorous and meaningful representation of the void size and shape distribution compared to the commonly used concept of void (pore) size distribution. Once again, a number of statistics (e.g., mean, mode, median, standard deviation) can be extracted from each chord-length distribution. It is also important to note that the chord length distribution can be extracted in different directions (orientations) for a given structure dataset, which allows one to quantify the anisotropy of the void size and shape distribution. For the MPL microstructure studied here, chord length distributions were extracted only for the void phase in the three primary orthogonal directions.

The method we have used in this study for determining the three orthogonal chord length distributions is very efficient for handling large 3-D microstructure datasets. The algorithm can be implemented "in place" so that no copy of the 3-D volumetric data needs to be created and thus the memory requirements for this approach are extremely low. Similarly, the computational time requirements grow linearly with size of the dataset in terms of voxels. The general method involves scanning voxel by voxel along the image in the direction of the chords of interest. When we encounter a voxel that contains the phase of interest (in our case, void space), we mark a flag and start a counter that keeps track of how many pixels we have encountered. Once a voxel that does not contain the phase of interest is encountered, the flag is flipped and the value of the counter is recorded as the length of one chord that has been found. After processing every pixel in the image only once, all the chords in a given direction can be determined. A distribution of these lengths can then be calculated with traditional means.

For cases where we are interested in chords that are parallel to the image axes, this method provides fast computation because we can simply scan along the columns and rows of the image. When the desired chord orientation is not one of these directions, the rotation of the 3-D volumetric image can be performed so that the desired direction would be aligned with one of the image axes to perform the same procedure above. Even with the addition of the rotation to the above presented algorithm, the computational time and memory complexity of the algorithm remain the same. Additionally, the proposed algorithm can work efficiently on chunks of large datasets as well as different chord directions of interest at a minimum computational cost. For the simplicity, the chord length distributions shown in this study are only the three orthogonal directions which coincide with the volumetric image axes so that no such rotation of dataset was necessary.

Estimation of structural diffusivity coefficient.— The topology of the internal structure of a material is expected to play a dominating role in the diffusion of any selected species through the sample. As such, variations in the key structure metrics discussed above can have significant impact on the transport characteristics of the material. For

Table I. Key structural properties of the MPL predicted using different sets of random volumes, each 100 × 100 × 100 pixels^3 (∼1 μm^3).

Metrics	Number of Random Volumes				Units
	80	100	200	300	
Porosity	0.41 ± 0.04	0.41 ± 0.04	0.41 ± 0.04	0.42 ± 0.04	Fraction
Total Surface Area	23.94 ± 2.70	24.13 ± 2.80	24.08 ± 2.46	24.21 ± 2.64	μm^2/μm^3
Pore Connectivity	0.99 ± 0.003	0.99 ± 0.003	0.99 ± 0.003	0.99 ± 0.003	Fraction
Structural Diffusivity Coefficient	0.22 ± 0.05	0.23 ± 0.04	0.22 ± 0.05	0.23 ± 0.05	Numeric

instance, the tortuosity and void size distribution can vary significantly with small variations in the manufacturing processes, which will in turn greatly affect the species diffusion within the material. Therefore, it is reasonable to assume that each material possesses a unique diffusivity characteristic, which can be represented by a specific structural diffusivity coefficient, K, to estimate the effective diffusivity, D_{eff}, of the species:

$$D_{eff} = K \cdot D_{i,j} \qquad [1]$$

where $D_{i,j}$ is the diffusivity of species i in species j.

A diffusion model was developed to extract the structural diffusivity coefficient from 3-D microstructure datasets. The model is based on a finite volume approximation to the steady state Fickian diffusion model. Each voxel of the microstructure dataset was treated as a finite volume, and was assigned a value of $D_{i,j}$ depending on whether it represented the void or the solid phase. The net flux for each voxel was maintained at zero. Dirichlet boundary conditions in the form of uniform concentrations were applied to the top and bottom surfaces (i.e., start and end surfaces in extracting tortuosity distributions) to induce a specified overall concentration gradient, while periodic boundary conditions were applied to the remaining surfaces to prevent any net flux in the in-plane directions. The resulting system of equations was solved to compute the concentration field and the net flux through the selected structure dataset. From the computed value of the net flux, the effective diffusivity and the structural diffusivity coefficient (K) were easily recovered.

Results and Discussion

Estimation of key structural properties.— The metric analyses were performed on sets of randomly selected small volumes (each 100 × 100× 100 pixels, ∼1 × 1 × 1 μm) within the full dataset of 500 × 800 × 200 pixels. The use of smaller volumes also allowed for speedy execution of the structure metrics algorithms, since the run time scales rapidly with the selected window size of the dataset being processed. Four different groups of datasets (80, 100, 200, and 300 random volumes) were evaluated to gauge the change in predicted values of the structure metrics, and to determine the sufficient number of volumes for use in simulations so that the variation in the internal structure of the tested MPL sample can be accurately captured. Table I shows the key structure metric results (porosity, total surface area, and void connectivity) for the four different groups of datasets obtained from the MPL sample. The results show very small variation (less than 5%) between the predicted values of the properties for each group, indicating that the material structure is sufficiently sampled. For this study, we have selected the set of 300 *random* volumes for further analysis, since it contains more information regarding the measured microstructure of the tested MPL.

For the selected 300 random volumes, the connected component search algorithm predicts the connectivity of the voids as 99% ± 0.3%, indicating that almost the entire void volume is a single highly connected network with very few isolated pores. Therefore, it is very likely that a similar level of void connectivity can be seen in the entire MPL sample. The results indicate an overall porosity of 0.42 ± 0.04 for the tested MPL sample, which is is in good agreement with reported values in literature (0.4-0.6).[11,12,26,27] The variation in reported values can be attributed to differences in the manufacturing

process of the MPL materials tested in these studies. For instance, in a recent study, Ostadi et al.[11] reported the porosity value of 0.4 for a similar MPL sample, which shows a very good agreement with the ones predicted in this study.

The predicted high void connectivity and low porosity features of the MPL sample can be attributed to the manufacturing process of the MPLs. Essentially, the MPL is prepared as a slurry which contains carbon particles, polymeric binder, PTFE and alcohol. This slurry is coated on the macro-DM substrate as a thin-layer.[9,31] The tight packing of carbon particles during the coating process is expected to result in low void space and high connectivity within the same phases in the MPL.

Tortuosity distribution.— Using the shortest path algorithm described in the Methods and Computational Procedures section, the tortuosity distribution for each of the selected 300 random volumes was computed. In addition, for each volume, statistical values including the maximum, minimum, and effective ("average") tortuosity were determined based on the computed tortuosity distributions. The computed tortuous pathways and the resulting tortuosity distribution for one random volume are shown in Fig. 4a as an example. The same procedure was repeated for all of the selected 300 random volumes to determine an overall tortuosity distribution for the tested MPL microstructure (Fig. 4b). This comprehensive dataset was further utilized to compute the effective (average) tortuosity of the 300 random volumes, as shown in Fig. 5. For comparison, the same procedure was performed on the other datasets (80, 100, and 200 random volumes), and the results are summarized in Table II.

When the maximum and minimum values in Table II are compared for each dataset, the computed tortuosity values range from 1.04 to 1.82 with an effective tortuosity value of ∼1.33. These results show that the tested MPL microstructure contains a broad range of tortuous paths with different lengths, which suggests that the use of a "single" effective tortuosity value alone may mislead the representation of the tortuous structure of the MPL, and therefore lead to an inaccurate estimate of the transport characteristics of the MPL. An appropriate approach, however, would be to represent the tortuous structure as a distribution (Fig. 4), where one can closely observe the trend and peaks in tortuous paths to identify the local regions that are highly resistive to the species transport. The shortest path search algorithm presented in this study has generated the tortuosity distribution in Fig. 4a based on rigorous analysis of approximately 1700 tortuous paths within the measured dataset. The computed tortuosity distribution shown in Fig. 4b based on all 300 random volumes indicates that the tortuous paths within the MPL structure are heavily concentrated on tortuosity values of 1.1 to 1.6 with an average tortuosity of 1.33. Such variation in the tortuosity suggests the existence of various connected paths with different resistances, which further complicates the task of describing the transport inside the MPL. It is also noteworthy to mention that the tortuosity distribution shown in Fig. 4b is cropped at a value of ∼2 for presentation purposes, since the data points beyond this value are very few and relatively insignificant in terms of overall statistics. However, the full distribution contains tortuosity values as high as ∼3.5.

In terms of comparison, the tortuosity values reported for the MPL in literature are typically within the range of 1.3 to 1.6.[11] The recent study by Ostadi et al.[11] reported the through-plane tortuosity value

a)

One Random Volume

**Computed Shortest Tortuous Paths
in the Measured Microstructure**

$\tau_{eff} = \tau_{avg} = 1.42$
St. Dev. = 0.37

*Based on a Single
Random Volume*

b)

$\tau_{eff} = \tau_{avg} = 1.33$
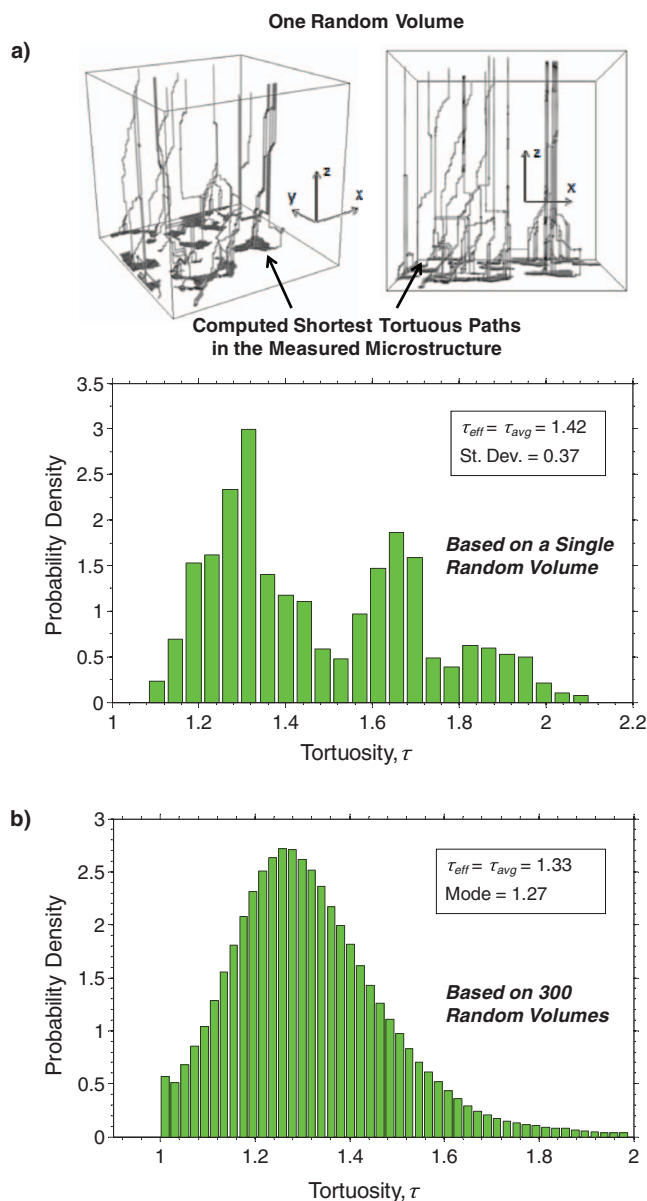Mode = 1.27

*Based on 300
Random Volumes*

Figure 4. a) Tortuosity distribution for one random volume (size 100 pixels³) selected from the full dataset. b) Overall tortuosity distribution of the MPL microstructure dataset based on the data computed for 300 random volumes.

for an MPL as 1.36, which shows a good agreement with the average value (~1.33–1.34) predicted in this study (Table II).

Chord length distribution.— The chord length distribution algorithm described in the Methods and Computational Procedures section was applied to the *full dataset* ($800 \times 500 \times 200$ pixels) to capture the
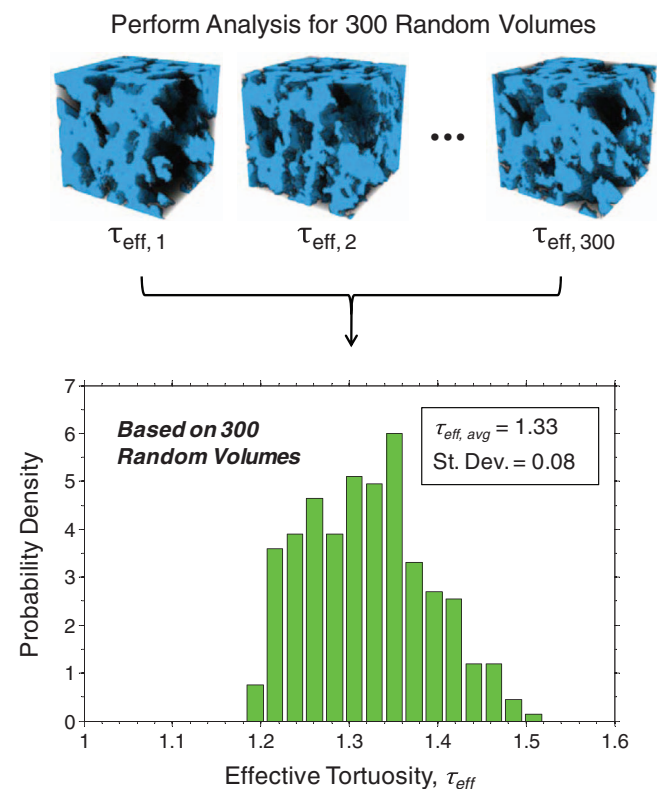
Perform Analysis for 300 Random Volumes

$\tau_{eff,\,1}$ $\tau_{eff,\,2}$ $\tau_{eff,\,300}$

$\tau_{eff,\,avg} = 1.33$
St. Dev. = 0.08

*Based on 300
Random Volumes*

Figure 5. Distribution of effective tortuosity (τ_{eff}) for 300 random volumes (each of size 100 pixels³) from within the full MPL microstructure dataset.

size of the void space within the MPL microstructure. The resulting chord length distributions are shown in Fig. 6a. As mentioned earlier, since the concept of a chord length distribution is not based on the assumption of idealized circular/spherical geometries as it is in conventional pore size analysis, the three primary orthogonal directions (x, y and z) were used as the possible chord orientations in these simulations to capture the irregular void geometry within the measured microstructure.

The computed chord length distributions (Fig. 6a) indicate that the MPL structure exhibits a void size ranging from 10 nm to 1 μm. The high percentage of measured chord lengths is observed to be below 200 nm (Fig. 6a), indicating that mass transport can be greatly inhibited in the MPL. Figure 6a also shows that the tested MPL has a higher percentage of small pores for the through-plane orientation, indicating the existence of anisotropy in pore structure in the orthogonal directions.

In addition to the identification of void size and distribution within the microstructure, the computed chord length data can be used to calculate dominant length scales to determine the mode of the transport within the microstructure. For instance, with the average chord length distribution data (Fig. 6a), one can calculate the Knudsen number and its distributions for hydrogen, oxygen, and water vapor in the MPL

Table II. Estimated maximum, minimum, and effective tortuosity of the MPL using different sets of random volumes, each $100 \times 100 \times 100$ pixels³ (~1 μm³).

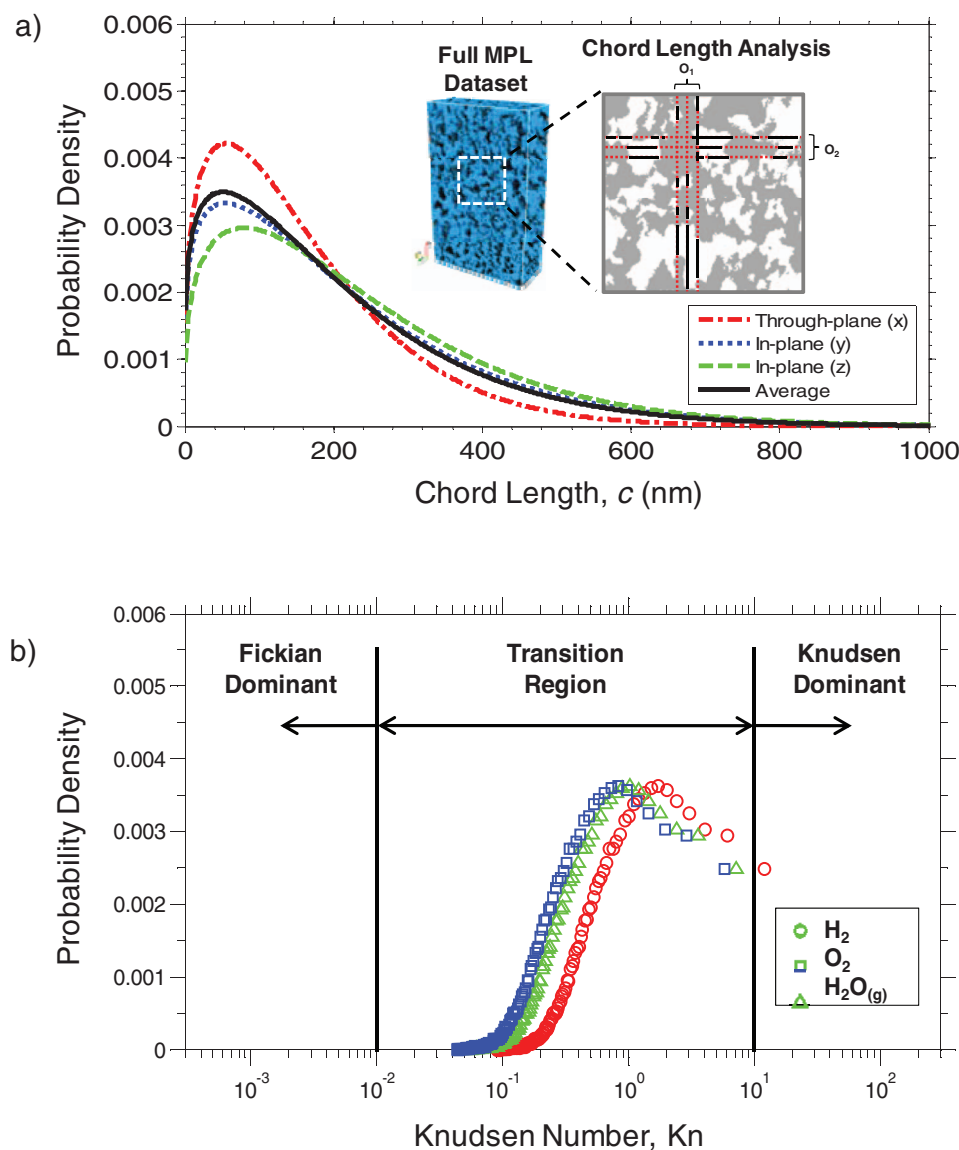| Metrics	Number of Random Volumes				Units
	80	100	200	300	
Maximum Tortuosity	1.82 ± 0.25	1.82 ± 0.28	1.74 ± 0.26	1.80 ± 0.24	Ratio
Minimum Tortuosity	1.05 ± 0.07	1.05 ± 0.05	1.08 ± 0.07	1.04 ± 0.05	Ratio
Effective Tortuosity	1.34 ± 0.09	1.33 ± 0.07	1.34 ± 0.11	1.33 ± 0.08	Ratio

Figure 6. a) Chord length distributions for the pore phase of the full MPL microstructure dataset in the three primary orthogonal directions and the average of the three distributions. b) Knudsen number distributions for hydrogen, oxygen, and water vapor in the MPL at 80°C and 1 atm, based on the computed average chord length distribution.

(Fig. 6b). The Knudsen number, Kn, is defined as the dimensionless ratio of the mean free path of fluid particles, λ, to the representative length scale, L:[3]

$$Kn = \lambda/L \qquad [2]$$

In this case, L is taken to be the chord length, and λ is calculated based on kinetic theory and by assuming an average relative particle velocity:[32,33]

$$\lambda = \frac{k_B T}{\sqrt{2}\pi d^2 P} \qquad [3]$$

where k_B is the Boltzmann constant, T is the temperature, and P is the pressure. The effective molecular diameter, d, is calculated using the appropriate covalent and van der Waals radii.[34,35] Accordingly, the effective molecular diameters of 302, 436, and 392 pm were calculated for H_2, O_2, and H_2O respectively, and the corresponding Knudsen number distributions for each species were determined based on the computed average chord length distribution (Fig. 6b). The Knudsen number distributions shown in Fig. 6b indicate that the majority of diffusion in the MPL for all three gas species falls in the transition region between continuum/slip flow and free-molecule flow (0.01 < Kn < 10), where both Fickian and Knudsen diffusion are prominent.[36,37]

This means that gas transport within the small pores of the MPL can be significantly influenced by molecular collisions with the pore walls.[38] Therefore, when modeling the species transport in fuel cell materials with relatively small void size distributions like the MPL, the wall interaction should be taken into consideration to achieve the most accurate results.[38,39]

Structural diffusivity coefficient.— Using the diffusion model described in the Methods and Computational Procedures section, the species diffusion was simulated for the 300 random volumes (Fig. 7a). A structural diffusivity coefficient was determined for each of the selected 300 random volumes to obtain a statistical distribution of the structural diffusivity coefficient for the full MPL dataset (Fig. 7b). The resulting distribution was averaged to determine an effective diffusivity coefficient that represents the diffusion characteristics of the tested MPL sample. For comparison, the same procedure was repeated for 80, 100 and 200 random volumes, and the results are tabulated in Table I.

As shown in Table I, the effective (average) structural diffusivity coefficient predicted for different dataset sizes (i.e., 80, 100, 200, and 300) ranges from 0.22 to 0.23, indicating that a sufficient microstructure dataset was sampled to capture the spatial heterogeneity
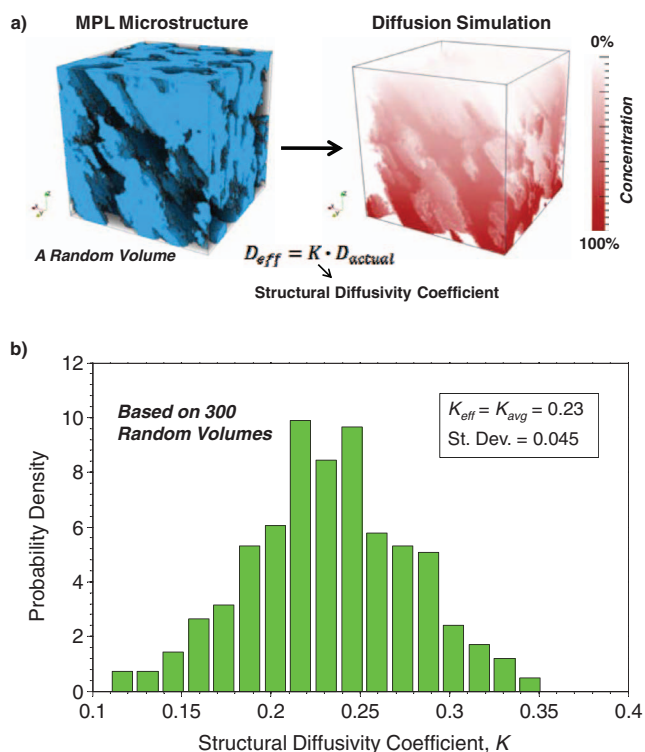
Figure 7. a) Diffusion simulation performed on the 300 random volumes from within the full MPL microstructure dataset. Each volume is 100 pixels³ in size. The structural diffusivity coefficient, K, is determined for each tested volume. b) Computed structural diffusivity coefficient distribution for the full dataset.

within the MPL structure. When the distribution in Fig. 7b is analyzed, the diffusivity coefficient varies from 0.12 to 0.35 with an average of 0.233, indicating the existence of local diffusion paths with different resistances due to the spatial heterogeneity within the MPL microstructure.

To date, most PEFC models utilize effective medium approximations (e.g., Bruggeman relation) to determine the effective diffusivity of a species as a function of bulk material properties such as porosity (ε) and tortuosity (τ). In these traditional approximations, the effective diffusivity (D_{eff}) of a species i, is typically described as:

$$D_{eff,i} = D_{abs,i} \frac{\varepsilon}{\tau} \qquad [4]$$

where D_{abs} represents the absolute diffusivity of a species i.[3] For further simplification, tortuosity and porosity are typically related with each other by using the Bruggeman relation:[3]

$$\tau = \varepsilon^{-0.5} \qquad [5]$$

which simplifies Eq. 5 into the form:

$$D_{eff,i} = D_{abs,i} \varepsilon^{1.5} \qquad [6]$$

While simple and quite convenient, Eq. 6 represents idealized geometries which may not adequately capture the true complex structure of fuel cell materials. For instance, Eq. 5 was originally derived for packed beds of spherical particles,[39] and therefore it is very unlikely that it can accurately account for the irregular void geometries that exist in fuel cell MPLs. In this study, the computed average structural diffusivity coefficient (Eq. 7 and Table I) was compared against those predicted by Eq. 4 and Eq. 6 to evaluate the effectiveness of the traditional approximations which are commonly used in PEFC models.

$$K = \frac{D_{eff,i}}{D_{abs,i}} \qquad [7]$$

If the computed average tortuosity and porosity shown in Table I and II are considered, the traditional approximations (Eq. 4 and 6) yield estimates of 0.32 and 0.27 for the structural diffusivity coefficient respectively, which are 37% and 18% higher than the diffusivity coefficient predicted by the present diffusion model. The estimates obtained by Eqs. 4 and 6 are also in considerable disagreement with each other. These discrepancies bring the validity of effective medium approximations such as Eqs. 4 and 6 into question for use in describing the transport in fuel cell materials. The results indicate that the direct use of these traditional approximations for fuel cell MPL can result in significant over-prediction of species diffusion; therefore when used in PEFC models, they will cause inaccuracies in model predictions. Therefore, for improved model accuracy, these traditional correlations need to be calibrated to properly account for the effects of internal structure of the fuel cell materials.

It is noteworthy to mention that as suggested by the chord length distribution data, species transport through the MPL is governed *partially* by Knudsen diffusion, which is not accounted for in the present diffusion model. However, since Eqs. 4 and 6 are independent of the length scale, the analysis regarding the potential issues associated with the use of effective medium approximations is still valid. Since the influence of wall interactions is not accounted for in the present diffusion model, it is very likely that the true structural diffusivity coefficient would be slightly lower than the one predicted by the present diffusion model. A lower structural diffusivity coefficient would further increase the error margin of the traditional approximations given by Eqs. 4 and 6.

Conclusions

In this paper, several "direct" microstructure analysis tools for the estimation of key structure-related metrics of porous fuel cell materials were presented. For initial demonstration, these methods were applied to a 3-D microstructure dataset of an MPL substrate of a PEFC.

Two important metrics, namely tortuosity distribution and chord length distribution, were introduced. Rather than a single tortuosity value, representation of the tortuous paths as a "distribution" is shown to be more effective to better understand the spatial variation of microstructure and the tortuous nature of fuel cell materials. Secondly, the chord length distribution metric is presented as an alternative concept for describing the void size distribution for this class of materials. This key metric represents the orientation and size related statistics of a desired phase (e.g., void, solid) in a 3-D microstructure dataset. It allows for the investigation of structural anisotropy and enables a more accurate analysis of irregular pore geometries in complex microstructures, where defining a void and its size is highly ambiguous such as in most fuel cell materials. The chord length analysis also enables direct quantification of the specific pore feature sizes, which can be used for determination of the dominant diffusion mode (e.g., Fickian or Knudsen) within the microstructure of the material.

Finally, a Fickian diffusion model was developed to determine the structural diffusivity coefficient of the tested MPL sample based on the measured microstructure. The results indicate that the direct use of effective medium approximations (e.g., Bruggeman relation), which is commonly practiced in most PEFC models, is not sufficient to accurately describe the species diffusion within the MPL internal structure. Similar conclusions can also be drawn for other fuel cell materials due to the similarity of their internal structures. Therefore, for improved model predictions, the traditional approximations need to be calibrated to better reflect the effects of microstructures of fuel cell materials on species transport and cell performance.

The microstructure analysis algorithms described in this study are not case or application specific. They can be used to determine the difficult-to-measure key structure-related transport properties in other porous materials that are used in different applications (e.g., batteries, supercapacitors etc), provided that high resolution images that clearly show the structural features of the materials are captured by FIB-SEM or other imaging techniques.

References

1. R. Borup, J. Meyers, B. Pivovar, Y. S. Kim, R. Mukundan, N. Garland, D. Myers, M. Wilson, F. Garzon, D. Wood, P. Zelenay, K. More, K. Stroh, T. Zawodzinski, J. Boncella, J. E. McGrath, M. Inaba, K. Miyatake, M. Hori, K. Ota, Z. Ogumi, S. Miyata, A. Nishikata, Z. Siroma, Y. Uchimoto, K. Yasuda, K. Kimijima, and N. Iwashita, *Chemical Reviews*, **107**, 3904 (2007).
2. E. C. Kumbur, K. V. Sharp, and M. M. Mench, *Journal of Power Sources*, **176**, 191 (2008).
3. K. Jiao and X. Li, *Progress in Energy and Combustion Science*, **37**, 221 (2011).
4. N. Yousfi-Steiner, Ph. Mocoteguy, D. Candusso, D. Hissel, A. Hernandez, and A. Aslanides, *Journal of Power Sources*, **183**, 260 (2008).
5. T. Swamy, E. C. Kumbur, and M. M. Mench, *Journal of The Electrochemical Society*, **157**, B77 (2010).
6. A. Z. Weber and M. A. Hickner, *Electrochimica Acta*, **53**, 7668 (2008).
7. H. Bajpai, M. Khandelwal, E. C. Kumbur, and M. M. Mench, *Journal of Power Sources*, **195**, 4196 (2010).
8. U. Pasaogullari and C. Y. Wang, *Electrochimica Acta*, **49**, 4359 (2004).
9. R. P. Ramasamy, E. C. Kumbur, M. M. Mench, W. Liu, D. Moore, and M. Murthy, *International Journal of Hydrogen Energy*, **33**, 3351 (2008).
10. N. S. K. Gunda, H. W. Choi, A. Berson, B. Kenney, K. Karan, J. G. Pharoah, and S. K. Mitra, *Journal of Power Sources*, **196**, 3592 (2011).
11. H. Ostadi, P. Rama, Y. Liu, R. Chen, X. X. Zhang, and K. Jiang, *Journal of Membrane Science*, **351**, 69 (2010).
12. J. Becker, C. Wieser, S. Fell, and K. Steiner, *International Journal of Heat and Mass Transfer*, **54**, 1360 (2011).
13. H. Iwai, N. Shikazono, T. Matsui, H. Teshima, M. Kishimoto, R. Kishida, D. Hayashi, K. Matsuzaki, D. Kanno, M. Saito, H. Muroyama, K. Eguchi, N. Kasagi, and H. Yoshida, *Journal of Power Sources*, **195**, 955 (2010).
14. Y. S. Wu, L. J. van Vliet, H. W. Frijlink, and K. van der Voort Maarschalk, *European Journal of Pharmaceutical Sciences*, **28**, 433 (2006).
15. S. Zils, M. Timpel, T. Arlt, A. Wolz, I. Manke, and C. Roth, *Fuel Cells*, **10**, 966 (2010).
16. Z. Fishman and A. Bazylak, *Journal of The Electrochemical Society*, **158**, B247 (2011).
17. S. Haussener, P. Coray, W. Lipinski, P. Wyss, and A. Steinfeld, *ASME Journal of Heat Transfer*, **132**, 023305 (2010).
18. W. B. Lindquist, S. M. Lee, D. A. Coker, K. W. Jones, and P. Spanne, *J. Geophys. Res.*, **101B**, 8297 (1996).
19. M. Axelsson and S. Svensson, *Pattern Anal. Applic.*, **13**, 159 (2010).
20. C. Ziegler, S. Thiele, and R. Zengerle, *Journal of Power Sources*, **196**, 2094 (2011).
21. E. A. Wargo, A. C. Hanna, A. Cecen, S. R. Kalidindi, and E. C. Kumbur, *Journal of Power Sources*, **197**, 168 (2012).
22. V. Pastushenko, SURFIT (http://www.mathworks.com/matlabcentral/fileexchange/6-244), MATLAB Central File Exchange (18 Nov 2004).
23. G. H. Ball and D. J. Hall, Isodata, Stanford Research Institute, Menlo Park, CA, Technical Report AD 699616 (1965).
24. T. W. Ridler and S. Calvard, *IEEE Transactions: Systems, Man, and Cybernetics*, **SMC-8**, 630 (1978).
25. D. Ramachandram, Automatic thresholding (http://www.mathworks.com/matlabcentral/fileexchange/3195), MATLAB Central File Exchange (31 Mar 2003).
26. K. T. Cho and M. M. Mench, *Journal of Power Sources*, **195**, 6748 (2010).
27. H. Tang, S. Wang, M. Pan, and R. Yuan, *Journal of Power Sources*, **166**, 41 (2007).
28. E. W. Dijkstra, *Numerische Mathematik*, **1**, 269 (1959).
29. S. Torquato and B. Lu, *Physical Review E*, **47**, 2950 (1993).
30. S. R. Niezgoda and S. R. Kalidindi, *Computers, Materials & Continua*, **14**, 79 (2009).
31. M. M. Mench, *Fuel Cell Engines*, John Wiley & Sons, Hoboken, New Jersey, 2008.
32. Mean free path, molecular collisions, 16 June 2011, <http://hyperphysics.phy-astr.gsu.edu/hbase/kinetic/menfre.html>.
33. N. M. Laurendeau, *Statistical Thermodynamics: Fundamentals and Applications*, Cambridge UP, Cambridge, 2005.
34. A. Bondi, *Journal of Physical Chemistry*, **68**, 441 (1964).
35. B. Cordero, V. Gómez, A. E. Platero-Prats, M. Revés, J. Echeverría, E. Cremades, F. Barragán, and S. Alvarez, *Dalton Transactions*, **21**, 2832 (2008).
36. X. Chen and E. Pfender, *Plasma Chemistry and Plasma Processing*, **3**, 97 (1983).
37. L. P. Yarin, A. Mosyak, and G. Hetsroni, *Fluid Flow, Heat Transfer and Boiling in Micro-Channels*, Springer, Berlin/London, 2008.
38. A. Berson, H. W. Choi, and J. G. Pharoah, *Physical Review E*, **83**, 026310 (2011).
39. J. G. Pharoah, K. Karan, and W. Sun, *Journal of Power Sources*, **161**, 214 (2006).